Physical Chemistry Chemical Physics 22.35 (2020): 19573-19584

DOI: https://doi.org/10.1039/D0CP02839H

PCCP

ROYAL SOCIETY OF CHEMISTRY

ARTICLE TYPE

Cite this: DOI: 10.1039/xxxxxxxxxx

A classical and semiclassical study of collisions between X^{q+} ions and water molecules

Clara Illescas[a], M. A. Lombana[a], L. Méndez,[a,*], I. Rabadán[a] and Jaime Suárez, [a‡]

Received Date
Accepted Date

DOI: 10.1039/xxxxxxxxxx

www.rsc.org/journalname

Collisions of He^{2+}, Li^{3+} and C^{3+} ions with water molecules are studied at energies ranging between 20 keV/u and 500 keV/u. Three methods are employed: the classical trajectory Monte Carlo (CTMC), the expansion of the scattering wave function in terms of asymptotic frozen molecular orbitals (AFMO) and a lattice method to numerically solve the time-dependent Schrödinger equation (GridTDSE). Total cross sections for single ionization, single electron capture, transfer ionization and electron production are calculated and compared with previous close-coupling calculations and experiments. The fragmentation branching ratios are discussed.

1 Introduction

Ion-water collisions at energies of several keV/u lead to the electron loss from water molecules, either by ionization or electron capture. Given that water is the main constituent of living tissues, these electron-loss processes are the first steps of the damage of biological systems by interaction with ions. Specifically, an important part of the cell damage is caused by the interaction of the DNA constituents with low-energy electrons released in collisions with water.[1] Moreover, the water cations can dissociate yielding ions and radicals that, in a second stage, interact with other biomolecules. From an applied point of view, ion interaction with water is relevant in cancer ion therapy, where the tissues are irradiated with fast beams of ions (H^+, C^{6+})[2,3]. On the other hand, the interaction of stellar wind ions with water molecules in cometary and planetary atmospheres produces electron capture and ionization processes. In the capture reaction between multiply charged ions, X^{q+}, and H_2O, the ions $X^{(q-1)+}$ are formed in excited states that can emit X-rays[4]. The relevance in these applications has motivated several experiments of ion collisions with water molecules[5–22] .

The ion-water collisions lead to the reactions:

$$X^{q+} + H_2O \longrightarrow X^{p+} + [H_2O]^{r+} + (p + r - q)e^- \qquad (1)$$

where $[H_2O]^{r+}$ indicates the different fragments with total charge $r+$, formed in the dissociation of the corresponding water cations. At the energies of the present work (20-500 keV/u), the characteristic collision time is below 0.25 fs and the molecule vibrations and rotations can be considered frozen since their periods are above 10 fs. Thus, we assume that the target nuclei are fixed at their equilibrium positions (Franck-Condon approximation). An extension of this idea leads to consider that the molecular fragmentation takes place following a two-step mechanism[16,23,24]: In a first step, one or more target electrons are released by interaction with the ion; in the second, the cations break up. In this respect, the wave packet simulation of Suárez *et al.* [25,26] shows that the dissociation of H_2O^+ requires more than 100 fs. This explains the success of some semiempirical works of fragmentation cross sections[23,27,28]. They involve the calculation of electron removal cross sections with fixed nuclei, which are then combined with the experimental fragmentation branching ratios, obtained in photoionization or electron impact ionization of water molecules.

Theoretical works for collision energies above 10 keV/u have applied the classical trajectory Monte Carlo (CTMC) method[27,29–34], the first Born approximation[17,35,36], the over-barrier model[?] +08 and the continuum-distorted-wave-eikonal-initial-state model[32,33,37–40]. The two-centre-basis-generator-method[20,28,41,42] (TC-BGM) has been applied to study collisions of H^+, He^+ and Li^{3+} ions with H_2O. Also, a lattice method was first applied by Errea *et al.* [43] to study $H^+ + H_2O$ collisions. All previously cited calculations were carried out within the framework of the independent electron approximation, where each electron moves in the average field created by the nuclei and the other electrons.

In the present work we consider collisions of ions with $q = 2, 3$ at energies above 20 keV/u. Previous works on these reactions include the experiments of Toburen *et al.* [8] and Rudd *et al.* [10] that reported the total cross section for the electron production (EP) process in $He^{2+} + H_2O$ collisions, measuring the number of electrons emitted in reaction (1). The total EP cross sections for this

[a] *Laboratorio Asociado al CIEMAT de Física Atómica y Molecular en Plasmas de Fusión. Departamento de Química, módulo 13, Universidad Autónoma de Madrid, 28049-Madrid, Spain.*

‡ Present address: Dipartimento di Chimica, Università degli Studi di Milano, 20133 Milano, Italy.

* E-mail: l.mendez@uam.es.

system were calculated by Illescas *et al.* [27] using the independent electron approximation and the CTMC method for treating the one-electron problem. The results of Illescas *et al.* [27] show good agreement with the experimental ones for $E > 50$ keV/u. The experimental work of Rudd *et al.* [10] also measured the total cross section for production of positive charges by target ionization and electron capture that we call target electron loss (EL). As we shall see, the calculated EL cross section provides a direct check on the accuracy of the one-electron methods. Unfortunately, similar experiments have not been carried out for ions with $q = 3$.

The CTMC calculation of Illescas *et al.* [27] yielded a cross section of electron capture in $He^{2+}+H_2O$ collisions that overestimated the experimental one, and, accordingly, it overestimated the EL cross section for $E < 50$ keV/u. The differences with the experiment can be due either to the application of the independent electron method or to a limitation of the classical treatment at low energies. In general the study of the validity of the CTMC treatment is relevant since the CTMC model yields one-electron cross sections without requiring very large computational resources. For instance, it allows us to consider several molecular orientations, without carrying out a prohibitively expensive calculation. As in the study of ion-atom collisions[44], we have considered a semiclassical alternative to calculate the EL and EP total cross sections for the $He^{2+}+H_2O$ system. This semiclassical calculation involves the direct numerical solution of the time-dependent Schrödinger equation (TDSE). We use the GridTDSE[45] code, originally designed for treating the propagation of a nuclear wave packet on a single potential energy surface. Here, as in the calculation of ionization in proton-water collisions[43], we obtain the time evolution of an electronic wave function in the (model) target and projectile fields. This calculation provides a useful check of the CTMC one, but it is difficult to apply it in a systematic way because the 3D numerical calculations require vast memory allocations.

A third alternative to solve the one-electron TDSE, is provided by the so-called asymptotic frozen molecular orbitals (AFMO) method; this is a semiclassical method, where the collision wavefunction is expanded in a set of molecular orbitals, obtained at large ion-molecule separations. In a previous work[31] for $H^+ + H_2O$ collisions, we showed that the CTMC and AFMO calculations of EP total cross sections and electron emission spectra agree for $E > 100$ keV/u. In the present work we have employed the AFMO method to calculate EP cross sections. As we shall explain in section 2, the present implementation allows us to apply the AFMO to calculate one-electron ionization probabilities at relatively high energies, but it does not simultaneously provide capture and ionization probabilities.

The one-electron transition probabilities, calculated with the above-mentioned methods, are then employed to obtain the ionization and capture probabilities for the many-electron system. tcredFor instance, the probability of single ionization of the molecule is obtained by adding the probabilities of ionizing one electron from each MO, without ionization from the other MOs. In the Independent Electron Model (IEM), the probabilities for the many-electron transitions are evaluated through multinomial expansions of the one-electron probabilities, which are calculated in a collision with a neutral target. When the probability of removing the first electron is high, one can think that successive electron removals will take place with lower probabilities than those calculated in the single-electron calculation. In this respect, previous works on proton collisions with water molecules pointed out that the IEM overestimates the probability of removing two electrons from different shells, and suggested that an alternative interpretation, called the Independent Event Model (IEV), could be more appropriate (see Jorge *et al.* [46] and references therein). Since both interpretations correspond to limit situations, it is difficult to predict *a priori* which one is more appropriate for a given process. However, the expressions for EP and EL in terms of the one-electron probabilities are the same in both IEM and IEV models[31,47], which permits to compare the EL and EP cross sections calculated with different one-electron methods between them and with the experiments.

Luna *et al.* [20] and Wolff *et al.* [21] performed experiments on Li^{3+} collisions with H_2O, but they did not report cross sections for EL or EP. Luna *et al.* [20] carried out TC-BGM calculations, which allow us a direct comparison with our calculations. The calculations on $Li^{3+}+H_2O$ are also relevant to compare with the $C^{3+}+H_2O$ system, which is particularly interesting because Luna and Montenegro [24] pointed out that the fragmentation branching ratios for this collision are completely different from those for $H^+ + H_2O$. Specifically, they found that H_2O^+, which is the dominant fragment in H^+ collisions, is not the main fragment in collisions with C^{3+} at $E > 100$ keV/u. This result was attributed to the importance of multiple electron removal processes but this point has not been confirmed so far by any calculation and will be elucidated in the present work.

The paper is organized as follows: In section 2 we introduce the methods applied in the calculations. In section 3 we present the results of the calculations. The cross sections for the net processes EL and EP in the three collision systems are compared with the experiments in subsection 3.1. A more detailed discussion of the computational methods is presented in subsection 3.2, where we display one.electron probabilities and collision histories. In subsection 3.3 we compare the cross sections for single capture and ionization with previous experiments and calculations for $Li^{3+}+H_2O$ collisions. A semiempirical model, based on the work of Murakami *et al.* [28], is applied in subsection 3.4 to relate our calculations with the experimental fragmentation branching ratios. Finally, we summarize our work in section 4.

Atomic units are employed unless otherwise stated.

2 Computational Methods

The methods employed in this work have been explained in detail in previous works and we only outline here some basic points required to discuss the results. At the energies of the present calculations, it is appropriate to apply the eikonal method (see e.g. Bransden and McDowell [48]) where the projectile follows rectilinear trajectories with velocity $\boldsymbol{v}$ and impact parameter $\boldsymbol{b}$:

$$\boldsymbol{R} = \boldsymbol{b} + \boldsymbol{v}t, \tag{2}$$

where $\boldsymbol{R}$ is the position vector of the ion nucleus with respect to the centre of mass of the molecular target. Explicit compar-

isons of quantal and semiclassical calculations[49] point out that the eikonal method is valid for collision energies above 250 eV/u. We also assume that the target nuclei remain in their equilibrium positions during the collision (Franck-Condon approximation). The equilibrium geometry is that reported by Hoy and Bunker[50]. In this respect, the work of Gabás *et al.*[51] considered ion-H_2O collisions with the sudden vibrational approximation, where the cross sections are obtained by averaging the cross sections calculated for a set of target nuclear positions, with weights given by the square of the ground-state vibrational wavefunction. These calculations indicate that the fixed nuclei approximation yields accurate results for $E > 1.5$ keV/u, which is very low compared with the energies of the present work.

The probabilities of different scattering events depend on the molecule orientation with respect to the projectile trajectory (or, equivalently, on the trajectory orientation with respect to a fixed target). Accordingly, one can consider several trajectory orientations following, for example, the scheme suggested by Illescas *et al.*[27], where the orientation averaged cross sections are evaluated using the 10 trajectory orientations sketched in Fig. 1. In the calculation the water molecule is on the XZ plane of the laboratory frame, and the arrows of Fig. 1 indicate the motion of the projectile. For instance, for trajectory t_4, $\boldsymbol{b} \parallel \hat{X}$ and $\boldsymbol{v} \parallel \hat{Y}$. The calculations of Illescas *et al.*[27] showed that the orientation-averaged total cross sections were very close to those of a single trajectory, specifically t_4. In this respect, one can note that the TC-BGM calculations of Luna *et al.*[20] considered two trajectory orientations (t_5 and t_9 in our notation).

The three calculations in this work rely on the use of the IEM, where the active electron moves in a one-electron potential that includes the Coulomb attraction by the ion core and a three-center model potential to describe the interaction of the active electron with the H_2O^+ core; it has the form:

$$V_{\rm mol}(\boldsymbol{r}) = V_{\rm O}(r_{\rm O}) + V_{\rm H}(r_{\rm H_1}) + V_{\rm H}(r_{\rm H_2}), \tag{3}$$

with $\boldsymbol{r}$ the electron position vector and $r_{\rm O}$, $r_{\rm H_1}$, $r_{\rm H_2}$ the electron distances to the nuclei of oxygen and hydrogen 1 and 2, respectively. The three terms are parameterized and fitted to the results of a previous self-consistent-field (SCF) calculation in a large gaussian basis set as detailed by Illescas *et al.*[27]

We have performed CTMC calculations for the system C^{3+}+H_2O, where we have included a model potential of the form:

$$V_{\rm C}(r_{\rm C}) = -\frac{Z-N_{\rm c}}{r_{\rm C}} - \frac{N_{\rm c}}{r_{\rm C}}(1+\alpha r_{\rm C})e^{-2\alpha r_{\rm C}} \tag{4}$$

to represent the interaction of the active electron with the C^{3+} ion, and where $r_{\rm C}$ is the distance of the electron to the C nucleus. In this expression $Z = 6$, $N_{\rm c} = 3$ is the number of core electrons and the parameter $\alpha = 1.851$ has been obtained by fitting the ionization energy of the C^{2+} ion.

In the CTMC model, the electron motion is described by a phase-space distribution. In this work we have employed an initial microcanonical distribution[52] for the active electron moving in the model potential. The distribution is discretized in terms of $N = 10^5$ electron trajectories that evolve independently up to

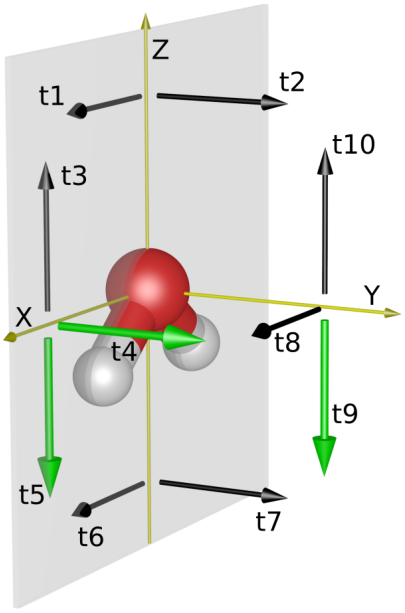

Fig. 1 Trajectory orientations employed in the present work. The trajectory orientation labelled t_4 is the representative trajectory orientation that yielded cross sections similar to the orientation-averaged ones in previous calculations[27]. The work of Luna *et al.*[20] considered the trajectory orientations labelled t_5 and t_9.

$t = t_{\rm max} = 500\,a_0/v$, when we calculate the one-electron probabilities for capture, $p^{\rm cap}$, and ionization, $p^{\rm ion}$, in the usual way:

$$p_k^{\rm cap} = \frac{N_{\rm cap}}{N};\; p_k^{\rm ion} = \frac{N_{\rm ion}}{N}; \tag{5}$$

here $N_{\rm cap}$ is the number of trajectories leading to electron capture (those with negative electron energy with respect to the projectile), $N_{\rm ion}$ is the number of trajectories leading to ionization (those with positive electron energy with respect to both target and projectile), and the k subscript labels the initial target molecular orbital ($1b_1$, $3a_1$, $1b_2$ or $2a_1$).

In the close-coupling and numerical treatments, the electron motion is treated quantum-mechanically. The corresponding wavefunction is an approximate solution of the semiclassical equation

$$h_{\rm el}\Psi_k(\boldsymbol{r},t;\boldsymbol{b},\boldsymbol{v}) = i\frac{\partial\Psi_k(\boldsymbol{r},t;\boldsymbol{b},\boldsymbol{v})}{\partial t}, \tag{6}$$

where $h_{\rm el}$ is the fixed-nuclei electronic hamiltonian that includes the model potential (3). Eqn (6) is formally identical to the TDSE. Initially, the electron motion is represented by a molecular orbital (MO), Φ_k, of H_2O and (6) must be solved with the initial condition

$$\Psi_k \underset{t\to-\infty}{\sim} \Phi_k(\boldsymbol{r})\exp(-i\varepsilon_k t) \tag{7}$$

with the origin of electronic coordinates placed in the center of mass of H_2O.

The AFMO model that we have used in here is the method I of Gabás *et al.*[51]. It consists on expanding Ψ_k as a linear combination of MOs, $\{\chi_k\}$, which are constructed on a basis set of GTOs $\{\xi_k\}$:

$$\chi_k(\boldsymbol{r};\boldsymbol{R}) = \sum_i c_{ki}(R_a)\xi_i(\boldsymbol{r},\boldsymbol{R}) \tag{8}$$

using the asymptotic coefficient matrix $\mathbf{C}(R_a)$, which is obtained by solving the secular equation for $h_{\rm el}$ in the $\{\xi_i\}$ basis set at a large distance R_a(=1000 a$_0$).

The scattering wave function is:

$$\Psi_k(\boldsymbol{r},t;\boldsymbol{b},\boldsymbol{v}) = \sum_l a_{kl}(t;\boldsymbol{b},\boldsymbol{v})\chi_l(\boldsymbol{r};\boldsymbol{R}) \exp\left(-i\int_0^t \varepsilon_l \,\mathrm{d}t\right) \qquad (9)$$

where $\varepsilon_l = (\mathrm{s}^{-1}\mathrm{h})_{ll}$, with s and h the overlap and hamiltonian matrices in the basis $\{\chi\}$.

The transition probabilities are now given by the asymptotic values of the coefficients a_{kl}, which are obtained by substituting (9) into (6). In practice, we have calculated the ionization probability as

$$p_k^{\rm ion} = \sum_l \mid a_{kl} \mid^2 \qquad (10)$$

where the sum extends over all the pseudostates; i.e., the MOs with $\varepsilon_l(R_a) > 0$. It must be noted that the expansion does not include electron translation factors. However, the use of a large gaussian basis set that produces 137 MOs with asymptotic positive energy and 73 MOs with negative one (50 located on the target, 23 on the projectile) allows to obtain accurate ionization cross sections, which will not be improved by adding any translation factor[53]. Errea *et al.*[31] discussed the limitation of the AFMO for H^++H_2O collisions. They found identical ionization total cross sections for $E > 60$ keV/u with a two-centre basis similar to that of (9) and with the one-centre basis obtained by keeping only the orbitals centred in the molecular nuclei. This result indicates that the interlocking of capture and ionization, which would lead to the overestimation of the ionization cross section, is not relevant at these energies. Nevertheless, the AFMO expansion is not appropriate to calculate electron capture cross sections.

In the lattice calculation, we consider a 3D Cartesian uniform grid of more than 46 million points with a 0.1 a$_0$ spacing, inside a cubic box of 36 a$_0$ side. We obtain the values of the initial wavefunction (7) at the points of this grid by applying the Lanczos algorithm[54] with the one-electron model-potential hamiltonian. The values of the discretized initial wavefunction are stored in a vector $\mathbf{\Psi}_k^{\rm M}$, which is then propagated by means of a second-order-difference scheme. A damping function[26] is added to the potential to avoid the nonphysical reflection of the wave packet at the box boundaries. The electronic density that leaves the box during the collision[43] yields the one-electron loss probability:

$$p_k^{\rm loss} = p_k^{\rm cap} + p_k^{\rm ion} = \lim_{t\to t_{\rm f}} \left[1 - \|\mathbf{\Psi}_k^{\rm M}\|^2\right], \qquad (11)$$

where $\|\mathbf{\Psi}_k^{\rm M}\|$ is the norm of the wavefunction $\mathbf{\Psi}_k^{\rm M}$ and $t_{\rm f}$ the final integration time.

To calculate $p_k^{\rm cap}$, we have extended the method employed by Jorge *et al.*[44]. In this calculation, the Li^{3+} projectile is fixed at the origin of electronic coordinates and the target molecule moves along a rectilinear trajectory. The initial electronic wave function is now given by the product of the molecular orbital χ_k and a plane-wave translation factor. With this alternative reference frame, the norm of the collision wavefunction at $t = t_{\rm f}$ yields $p_k^{\rm cap}$ and $p_k^{\rm ion} = p_k^{\rm loss} - p_k^{\rm cap}$. We have checked the convergence of the capture probabilities by carrying out exploratory calculations with an extended box of 44 a$_0$ and 0.08 a$_0$ spacing.

The three methods outlined above provide the transition probabilities $p_k^{\rm cap}$ and $p_k^{\rm ion}$ for the active electron moving in the model potential with a given initial condition. However, during the collision, all the electrons of the system can participate in non-adiabatic transitions. Following the notation of Luna *et al.*[20], the many-electron transition probabilities $P_{mn}^{\rm IEM}$ correspond to the process in which m electrons are captured and n electrons released; i.e., $m = q - p$ and $n = p + r - q$ in the notation of eqn (1). The probabilities $P_{mn}^{\rm IEM}$ are obtained by combining the IEM one-electron probabilities. For instance, the probability for ionizing one electron when the remaining electrons are neither captured nor ionized is:

$$P_{01}^{\rm IEM} = 2\sum_{k=1}^{4} p_k^{\rm ion} p_k^{\rm el} \prod_{j\neq k}^{4} (p_j^{\rm el})^2 = \sum_k P_{01}^{\rm IEM}(k)\,, \qquad (12)$$

where we only consider transitions from the valence orbitals of H_2O ($j,k \in \{1,2,3,4\} \equiv \{2a_1, 1b_2, 3a_1, 1b_1\}$), and where

$$p_k^{\rm el} = 1 - p_k^{\rm ion} - p_k^{\rm cap} = 1 - p^{\rm loss} \qquad (13)$$

is the probability that the electron remains bound to the target. Analogously, the probability of one target electron being captured while the rest of the electrons remain in the target is

$$P_{10}^{\rm IEM} = 2\sum_{k=1}^{4} p_k^{\rm cap} p_k^{\rm el} \prod_{j\neq k}^{4} (p_j^{\rm el})^2 = \sum_k P_{10}^{\rm IEM}(k)\,. \qquad (14)$$

If we move to the IEV model, the probability of removing a second electron from a different MO is neglected, $\prod_{j\neq k}(p_j^{\rm el})^2 \approx 1$, and the probabilities for single ionization ($P_{01}^{\rm IEV}$) and single electron capture ($P_{01}^{\rm IEV}$) are:

$$P_{01}^{\rm IEV} = 2\sum_{k=1}^{4} p_k^{\rm ion} p_k^{\rm el} \qquad (15)$$

$$P_{10}^{\rm IEV} = 2\sum_{k=1}^{4} p_k^{\rm cap} p_k^{\rm el} \qquad (16)$$

which are greater than the corresponding IEM probabilities (12) and (14) Similarly, the probabilities for the two-electron processes: transfer ionization (P_{11}), double ionization (P_{02}) and double capture (P_{20}) can be also obtained from the one-electron probabilities:

$$P_{11}^{\rm IEM} = 2\sum_{k=1}^{4} p_k^{\rm ion} p_k^{\rm cap} \prod_{j\neq k}^{4} (p_j^{\rm el})^2 + 4\sum_{k}^{4}\sum_{j\neq k}^{4} p_k^{\rm ion} p_j^{\rm cap} p_k^{\rm el} p_j^{\rm el} \prod_{l\neq k,j}^{4} (p_l^{\rm el})^2 \qquad (17)$$

$$P_{11}^{\rm IEV} = 2\sum_{k=1}^{4} p_k^{\rm ion} p_k^{\rm cap} \qquad (18)$$

and analogous expressions for P_{02} and P_{20}.

Finally, the cross sections for each process are obtained in the

standard way:

$$\sigma_{mn} = 2\pi \int_0^\infty bP_{mn}\mathrm{d}b\,. \tag{19}$$

In the IEM, the probability for EP is given by the simple expression:

$$P_{\mathrm{EP}}^{\mathrm{IEM}} = \sum_{m,n} nP_{mn}^{\mathrm{IEM}} = 2\sum_k p_k^{\mathrm{ion}} \tag{20}$$

and

$$\sigma_{\mathrm{EP}}^{\mathrm{IEM}} = 2\sum_k \sigma_k^{\mathrm{ion}} \tag{21}$$

where σ_k^{ion} is the one-electron ionization cross section, calculated by integrating bp_k^{ion}. Analogously, for the EL reaction

$$P_{\mathrm{EL}}^{\mathrm{IEM}} = \sum_{m,n} (m+n)P_{mn}^{\mathrm{IEM}} = 2\sum_k p_k^{\mathrm{loss}} \tag{22}$$

$$\sigma_{\mathrm{EL}}^{\mathrm{IEM}} = 2\sum_k \sigma_k^{\mathrm{loss}} \tag{23}$$

In the IEV model the expressions (21) and (23) also hold, although, obviously, the probabilities of processes involving the removal of more than two electrons vanish in this interpretation. Thus both interpretation differ in the branching ratios between different electron removal channels. Eqn (21) and (23) provide direct relationships, independent on the many-electron interpretation, between the measured cross sections for EP and EL[8,10], and the one-electron probabilities p_k^{ion} and p_k^{loss}.

3 Results and discussion.

3.1 Target electron loss and electron production

The calculated EL and EP total cross sections for $He^{2+}+H_2O$ are compared in Fig. 2 with the experimental data. The CTMC cross sections for EL are obtained from the probabilities of Illescas *et al.* [27] using eqn (22) and (23), and similarly the CTMC EP cross sections are evaluated using eqn (20) and (21). We have included in this illustration the orientation averaged cross sections and, in panel (a), we have also plotted the results for two trajectory orientations (t_2 and t_6) that correspond to the minimum and maximum values over the set of trajectory orientations of Fig. 1. It can be noted that the average value is practically identical to the cross section calculated for the trajectory orientation t_4, also shown in the figure. A second conclusion that can be drawn from this illustration is the good agreement between CTMC and GridTDSE calculations, which reinforces the validity of both computational models. It can be noted in Figs. 2 and 3 that the GridTDSE calculations are restricted to $E < 300$ keV/u because, as explained by Jorge *et al.* [44], the fast oscillation of the scattering wavefunction at high relative velocities requires the use of very dense grids.

Our EL cross sections show good agreement with the experimental ones for $E > 50$ keV/u while, for lower energies, the calculation overestimates the experimental values. This overestimate, already pointed out by Illescas *et al.* [27], is found in both classical and semiclassical calculations and, therefore, it is not due to a limitation of the CTMC method. On the other hand, the calculated and experimental EP cross sections of Fig. 2(b) agree at low energies, which might point to the need of a multielectronic description of the electron capture process at low energies. At

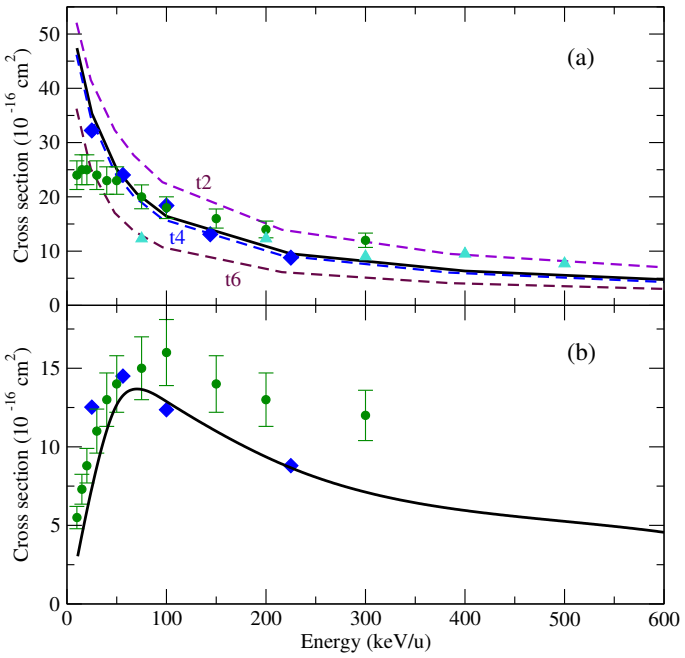

Fig. 2 Total cross sections for target electron loss (a) and electron production (b) in $He^{2+}+H_2O$ collisions. Present calculations: —, orientation-averaged CTMC ; - - -, CTMC results for EL for trajectory orientations t_2, t_4 and t_6, as indicated in the figure; ♦, t_4 GridTDSE; •, EL and EP experimental cross sections[10]; ▲, EL experimental data[8].

$E \gtrsim 150$ keV/u, where the electron capture is small, EL and EP cross sections are practically identical and we find a somewhat better agreement with the experiment of Toburen *et al.* [8]. There is a remarkable agreement with the experiment in the ionization threshold in Fig. 2.

Figure 3 shows the EL and EP total cross sections for collisions of Li^{3+} and C^{3+} with H_2O. As already pointed out for collisions with He^{2+}, we can observe the good agreement between CTMC and GridTDSE results for collisions with Li^{3+}. We find a small difference between the CTMC results for both ions with a somewhat higher contribution of the electron capture reactions for the dressed projectile. It must be noted that we plot in this figure the contribution to the EL and EP reactions of the target electrons, but the (probably small) loss of C^{3+} core electrons is not taken into account. The AFMO calculation provides an additional support of the other models at $E > 150$ keV/u. The limitations of this approach at lower energies are illustrated in Figure 3(b) where one can note the overestimate of the EP cross section because, as explained in section 2, the one-electron ionization and electron capture processes are not completely separated.

Although there are no direct measurements of EL and EP cross sections for $Li^{3+}+H_2O$ collisions, we can compare our results with the TC-BGM calculations and experiments reported by Luna *et al.* [20] by adding the values $n\sigma_{mn}$ and $(m+n)\sigma_{mn}$. In particular, the TC-BGM values of σ_{mn} were obtained by digitizing the figures of that paper, and the corresponding estimates of EL and EP cross sections are shown in Fig. 3. The agreement with our results is reasonable, and the differences at low energies could be explained by the lack of processes with $m+n > 4$ in the esti-

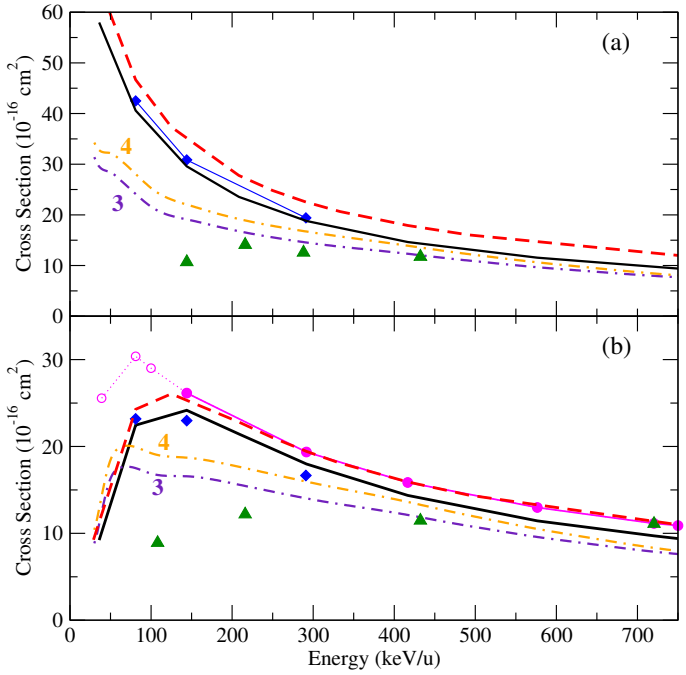

Fig. 3 Total cross sections for target electron loss (a) and electron production (b) in Li^{3+} and C^{3+} collisions with H_2O. Present calculations: —, orientation-averaged CTMC for Li^{3+} collisions; - - -, orientation-averaged CTMC results for C^{3+} collisions; ♦, t_4 GridTDSE for Li^{3+} collisions; —●—, t_4 AFMO for Li^{3+} collisions. ▲, experimental results of Luna *et al.*[20] for Li^{3+} collisions. The TC-BGM results of Luna *et al.*[20] for Li^{3+} collisions are indicated by dashed-dotted lines. The lines labelled 3, are obtained by adding the contributions up to three-electron processes ($m+n \leq 3$) in eqns. (20) [panel (a)] and (22) [panel (b)]. Analogously, the lines labelled 4 include up to four-electron processes ($m+n \leq 4$).

mate of the TC-BGM cross sections from the published data. The large contribution of processes with $m+n > 3$, is probably a consequence of the IEM, as pointed out by Kovács *et al.*[33]. Similarly, we have estimated the experimental cross section by the weighted sum of the experimental[20] cross sections σ_{mn} tabulated in that paper. In contrast with the good agreement between calculations and experiments for He^{2+} collisions (Fig. 2), we find that the energy dependence of the experimental values is different from the theoretical ones. This discrepancy might come from the way the experiments were performed. Luna *et al.*[20] measured the cross sections for the formation of different fragments, and it is not easy to assign the formation of given fragments, e.g. H^+ or OH^+, to a reaction that removes a specific number of electrons. However, calculations and experiment converge to similar cross sections at high energies.

3.2 One-electron probabilities

To gain insight into the comparison of the calculation models, we display in Fig. 4 the one-electron transition probabilities $p_k^{\rm cap}$ and $p_k^{\rm ion}$ from the CTMC, GridTDSE and AFMO calculations for $Li^{3+}+H_2O$ collisions. We have considered an intermediate energy ($E = 144$ keV/u) of the energy interval considered, where the three calculations of EP cross section agree. One can note that the shapes and heights of the opacity functions $bp_k^{\rm cap}(b)$ and $bp_k^{\rm ion}(b)$ for these calculations are similar, but there are some discrepancies. For example, GridTDSE and AFMO calculations yield lower ionization probabilities for $1b_1$ than for $1b_2$, while the reverse is found in the CTMC calculations. These differences stem from the nodal structure of the MOs, which is not present in the corresponding CTMC initial distributions. The orbital $1b_1$ is similar to the orbital $2p_y$ of the oxygen atom; it vanishes on the molecular plane and it has two lobes with the maximum probability density along the Y direction, parallel to the projectile velocity in the t_4 trajectory. On the other hand, the MO $1b_2$ has two lobes oriented perpendicular to the trajectory and, for not too low b, the projectile trajectory crosses a region of larger electron density when the electron occupies this orbital rather than the $1b_1$. In the CTMC model, the initial electron densities do not show a nodal structure and, accordingly, the ionization probabilities are essentially dependent on the ionization energies; the b_1 ionization energy is smaller than the $1b_2$ one, leading to a higher ionization probability from the $1b_1$ MO. Similarly, the $3a_1$ MO has a nodal plane that contains the vector $\boldsymbol{v}$ when the projectile follows the trajectory t_4. Consequently, the GridTDSE and AFMO calculations yield smaller ionization probabilities than those from the CTMC calculations. In spite of the differences arising from the lack of nodal structure in the classical distribution, we find good agreement between CTMC and semiclassical results when transitions from all the valence MOs are taken into account (see Figs. 2 and 3).

There is a remarkable agreement between the two semiclassical calculations in Fig. 4, which supports both the basis set of the AFMO expansion and the grid used in the GridTDSE calculation. In particular, the two semiclassical calculations agree for the collision starting from the inner valence MO, $2a_1$, which indicates the the grid density employed in the numerical calculation accurately

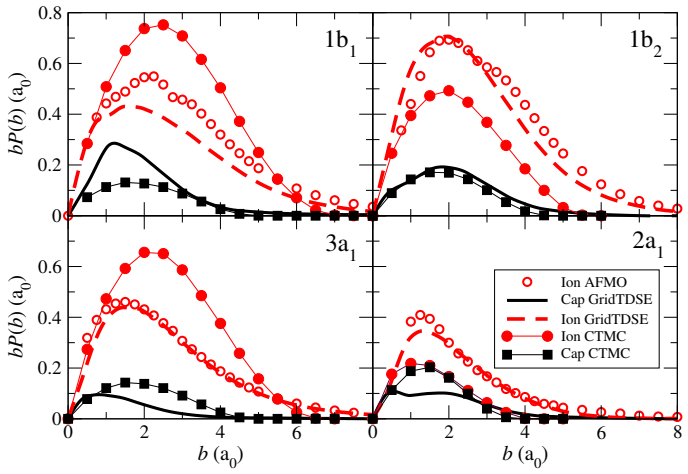

Fig. 4 Opacity functions for ionization, $bp^{\rm ion}$, and capture, $bp^{\rm cap}$, as functions of the impact parameter b, for the four valence MOs of H_2O (indicated in the panels), in Li^{3+}+H_2O collisions at $E = 144$ keV/u, and the trajectory orientation t_4. CTMC calculations (solid symbols), GridTDSE (solid and dashed lines) and AFMO (open symbols).

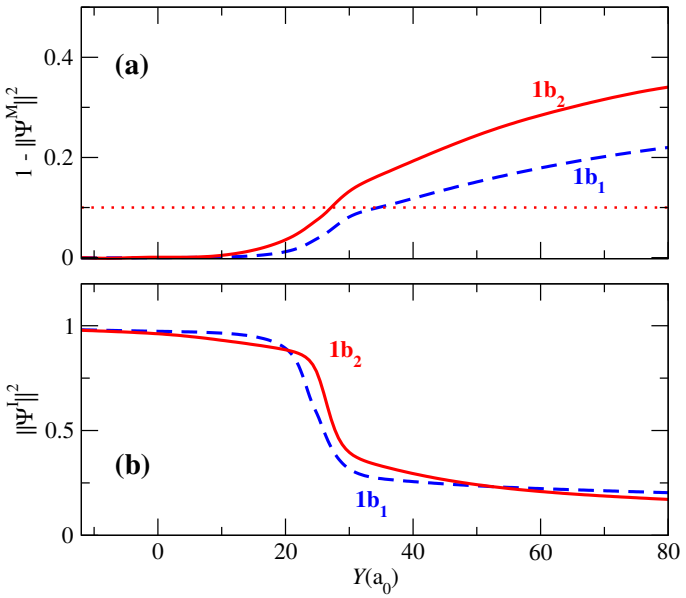

Fig. 5 Norms of the collision wavefunctions for $E = 144$ keV/u, $b = 2.0$ a_0, and trajectory orientation t_4 in Li^{3+}+H_2O collisions. The corresponding initial MOs are indicated next to the curves. The norms have been obtained in GridTDSE calculations of (a) electron loss, where the molecule is fixed at the center of the box and the norms are plotted as functions of the Y coordinate of Li^{3+}, (b) electron capture, where the projectile is fixed at the center of the box and the norms are plotted as functions of the position of the molecular center of mass along the trajectory. The dotted horizontal line in panel (a) is the asymptotic value of $\|\Psi^{\rm I}((1b_2)\|^2$.

represents this relatively compact orbital.

The orientation dependence of the capture probabilities is less marked; for instance, the capture from $1b_1$ takes place at low impact parameters that correspond to transitions at short projectile-target distances, where the above-mentioned difference of a smaller transition probability for trajectories parallel to the orbital orientation is no longer relevant; this can also be noted in the good agreement between CTMC and semiclassical transition probabilities at short b.

To further analyze the collision mechanism, we plot in Fig. 5 the collision histories obtained with the GridTDSE method for a representative trajectory with orientation t_4, $E = 144$ keV/u and $b = 2.0$ a_0, which approximately corresponds to the maxima of $bp^{\rm ion}(b)$ of Fig. 4. In the top panel of Fig. 5, we plot $1 - \|\Psi^{\rm M}_k\|^2$ [see eqn (11)] from the electron loss calculation, where the molecule is fixed at the center of the box and the Li^{3+} nucleus follows a rectilinear trajectory. The abscissas of this plot are the values of the projectile y-coordinate, $Y = \boldsymbol{R}\cdot\hat{\boldsymbol{v}}$. When the projectile leaves the box ($Y = 16$ a_0), we observe a decrease of the norm, $\|\Psi^{\rm M}_k\|$, which corresponds to the electron density that is temporarily bound to the projectile. After the projectile leaves the box, there is a slow diffusion of the electron density that is absorbed by the damping function when touches the wall of the box; this second process is describing ionization.

In the bottom panel of Fig. 5, we plot the squared norm of the wavefunction obtained when calculating capture probabilities. In this case, the projectile is fixed at the origin of coordinates and the molecule follows a straight-line trajectory. Accordingly, $\|\Psi^{\rm I}_k\|^2$ represents the electron density bound to Li^{3+}after the collision. One can note the step function shape of $\|\Psi^{\rm I}_k\|^2$ near the box limit, where the the electron density bound to the molecule leaves the box. One can also note that the asymptotic value of $\|\Psi^{\rm I}_k\|^2$ in panel (b) is similar to $1 - \|\Psi^{\rm M}_k(Y \approx 30)\|^2$ (around the first step) in panel (a), in agreement with our previous interpretation that it mainly corresponds to electron capture. It is also noticeable that the values of $\|\Psi^{\rm I}_k\|^2$ for both OMs are similar in panel (b).

The actual mechanism of the capture reaction is illustrated in Fig. 6; it shows contour plots of the electron probability density at the plane $Z = 0$ for trajectory t_4. In these graphs, the Li^{3+} nucleus is fixed at the origin and the molecule moves along the Y direction (see Fig. 1) with an impact parameter $b = 2.0$ a_0. Two snapshots are presented: one at the closest approach between projectile and target ($Y = 0$) and the other when the molecule has left the box ($Y = 28$ a_0). The evolution of the the $1b_1$ MO is illustrated in the left panels of this figure. Initially, the MO is very similar to the $2p_y$ orbital of oxygen, and at the point of closest approach ($Y = 0$) the MO is not distorted and the electron density near the Li^{3+} nucleus is small with the electron capture process taking place for $Y > 0$. However, the lobes of the $1b_2$ MO are in the X direction, they are perpendicular to the velocity vector. Since the Li^{3+} ion is closer to the tail of the electron density of the $1b_2$ MO than to that of the $1b_1$, the delocalisation from $1b_2$ is noticeable at $Y = 0$. We find that, for this trajectory orientation, the electron capture is faster from the $1b_2$ MO, but, as time goes on, the continuum delocalisation from $1b_1$ leads to analogous values of the norm for both orbitals, as shown in in the contour plots of Fig. 6 and also in the asymptotic values of the norms in Fig. 5(b). It can be noted that the capture from the MO $1b_1$ leads to a more diffuse wavefunction of Li^{2+}, illustrating the fact that the capture from the highest occupied MO is preferred into high-n atomic orbitals, which have similar energies.

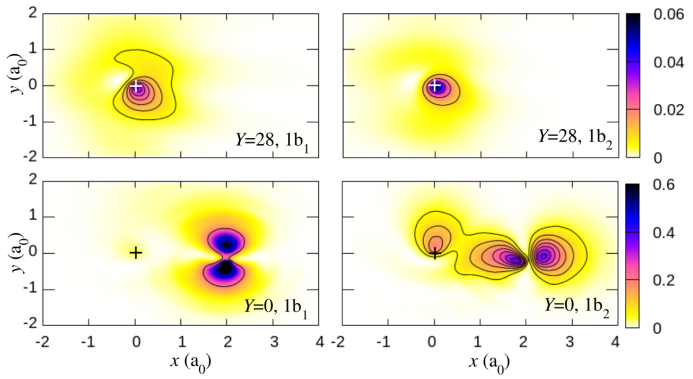

Fig. 6 Contour plots of $\|\Psi_k^{\rm cap}\|^2$ on the plane $Z=0$ at two positions of the molecule, $Y=0$ and $Y=28$ a_0. and the MOs $1b_1$ and $1b_2$, as indicated in the panels, for a trajectory t_4 with $b=2.0$ a_0 and $v=2.4$ a.u. ($E=144$ keV/u) in Li^{3+}+H_2O collisions. The color maps are the same for the panels with the same Y.

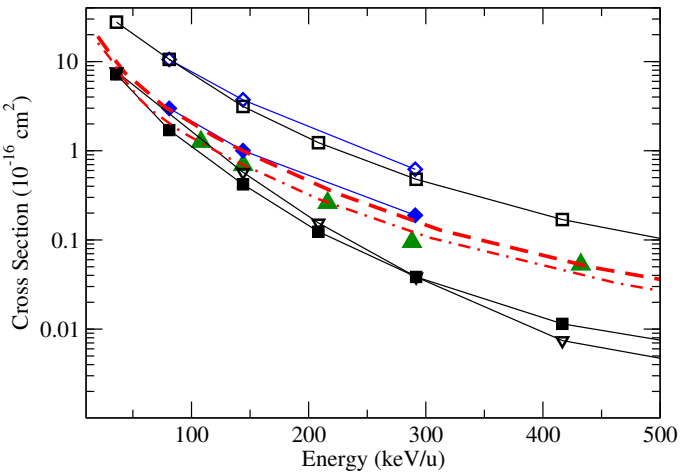

Fig. 7 Total cross section for single capture, σ_{10}, in Li^{3+}+H_2O collisions, as a function of the collision energy. Present calculations: —□—, orientation-averaged CTMC/IEV; —■—, orientation-averaged CTMC/IEM; —▽—, t_4 CTMC/IEM; —◇—, t_4 GridTDSE/IEV; —◆—, t_4 GridTDSE/IEM. Dashed line, TC-BGM[20], and dash-doted lines, TC-BGM without Auger emission[20]. ▲, experimental results (error bars are similar to the size of the symbols).

3.3 Cross sections for ionization and capture reactions

In Fig. 7 we plot the total cross sections for single electron capture $\sigma_{10}^{\rm IEM}$ and $\sigma_{10}^{\rm IEV}$, obtained by integrating the transition probabilities of eqn (14) and (16). Like in calculations[27] on H^++H_2O, we find good agreement between the single orientation t_4 and orientation-averaged results for CTMC calculations with both the IEM and IEV (not shown in the figure for clarity) many-electron models. We also find very good agreement between the CTMC/IEV and GridTDSE/IEV calculations. This agreement indicates that the CTMC method provides accurate orientation-averaged cross sections when taking into account the contribution of all MOs.

We have also plotted, in Fig. 7, the TC-BGM cross sections of Luna *et al.* [20], calculated without including the Auger correction, which show a very good agreement with our GridTDSE/IEM results. Given that both methods are completely different, the results are a good indication of their accuracy, which is confirmed by the agreement with the experimental cross sections. The TC-BGM calculation has also considered the Auger effect by subtracting from σ_{10} the contribution from the inner orbital $2a_1$, that is assumed to lead to Auger emission with probability equal to one, and finally leads to the transfer ionization reaction. The correction leads to a relatively small decrease of σ_{10}. We have applied the same idea to the GridTDSE result and the corrected cross section is indistinguishable from the one calculated including the contributions from the four valence orbitals.

The single ionization cross sections, $\sigma_{01}^{\rm IEM}$ and $\sigma_{01}^{\rm IEV}$, are presented in Fig. 8. As in Fig. 7, we include the GridTDSE cross sections calculated for the t_4 orientation, and orientation-averaged CTMC cross sections and the t_4 AFMO results.With the CTMC calculations, we have checked that the differences between orientation-averaged and t_4 results are small. The CTMC calculations show a large dependence on the many-electron interpretation, but both calculations lead to an energy-dependence of the cross section different from that of the experiment, with a better agreement of the experiment with the CTMC/IEM at low energies and with the CTMC/IEV at high energies. In this respect, the energy-dependence of the TC-BGM cross section is similar to that from our CTMC/IEM calculation, although the TC-BGM is always higher than our result. The comparisons of Figs. 7 and 8 indicate that the IEV interpretations leads to an overestimate of the one-electron removal cross sections.

The two semiclassical calculations, AFMO/IEM and GridTDSE/IEM, of σ_{01} show a reasonable agreement, but they do not display the maximum at $E\approx 50$ keV/u of the TC-BGM calculation. To further check these results, we have checked that the average of t_5 and t_9 AFMO cross sections is indistinguishable from those of t_4.

In both Figs. 7 and 8, we observe that there is a very good agreement between CTMC/IEV and GridTDSE/IEV cross sections, but there are some differences between the corresponding calculations with the IEM interpretation. This can be explained as a consequence of the orientation dependence of the transition probabilities that yield smaller values of the factors $\prod(p_j^{\rm el})^2$ (eqn (12) and (14)) in the CTMC calculation than in the semiclassical one. As an example, in Fig 4, the CTMC probabilities $p_j^{\rm el}$ are small for both $1b_1$ and $3a_1$; however, the corresponding GridTSE probabilities are larger, and accordingly the reduction of the contributions from the other orbitals are smaller.

Fig. 9 displays the transfer ionization cross sections (σ_{11}), where a similar energy dependence is found in the GridTDSE/IEM calculations, and the experimental and TC-BGM results. The behaviour of the CTMC/IEM is similar to that found in the Fig. 7: it agrees with the semiclassical calculations for $E\lesssim 200$ keV/u. In the energy range explored in the present GridTDSE calculation, no significant Auger contribution is found. The experimental cross sections are larger than the calculated ones by a factor between 1.5 and 2. These differences between experimental data and calculations could point to electron correlation effects that are obviously not included in IEM models; but, as mentioned by Luna *et al.* [20], the comparison between calculated and experimen-

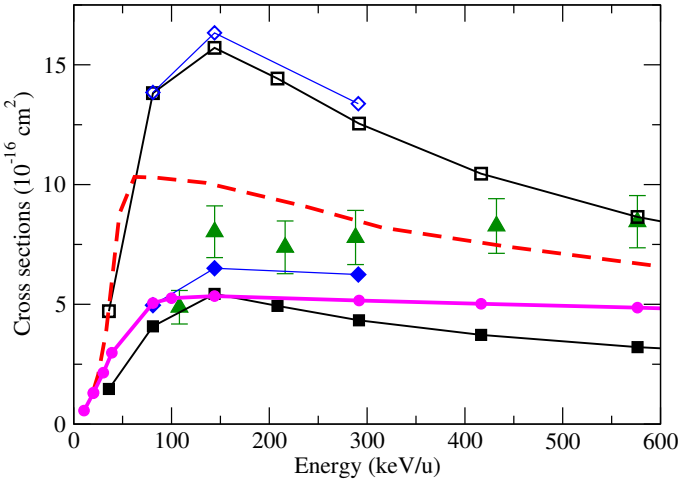

Fig. 8 Total cross sections for single ionization σ_{01}, in Li^{3+}+H_2O collisions, as a function of the collision energy. Present calculations: —□—, orientation-averaged CTMC/IEV; —■—, orientation-averaged CTMC/IEM; —◊—, t_4 GridTDSE/IEV; —♦—, t_4 GridTDSE/IEM; —●—, t_4 AFMO/IEM. Dashed line, TC-BGM without Auger emission[20]. ▲, experimental results[20].

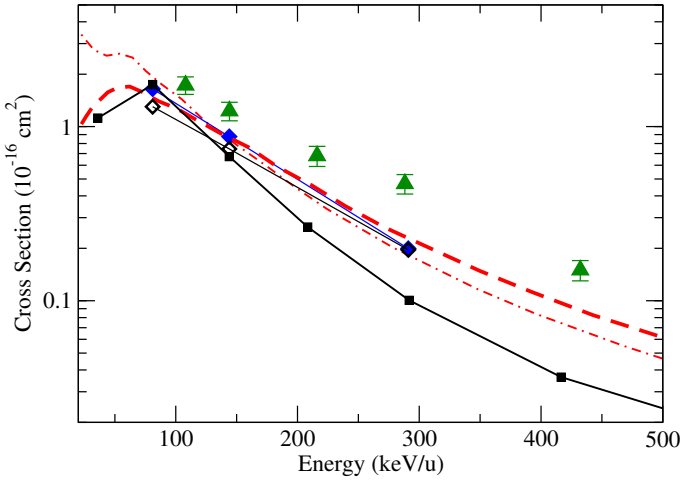

Fig. 9 Total cross sections for transfer ionization σ_{11}, in Li^{3+}+H_2O collisions, as a function of the collision energy. Present calculations: —■—, t_4 CTMC/IEM —♦—, t_4 GridTDSE/IEM; —◊—, t_4 GridTDSE/IEM without Auger emission. Thick dashed line, TC-BGM without Auger emission[20], thin dash-dotted line, TC-BGM[20] with Auger emission. ▲, experimental results[20].

tal results is not straightforward since the experiment cannot distinguish between protons originated in single or multiple electron removal processes.

3.4 Fragmentation cross sections

In this section we estimate the cross sections for production of H_2O^+ and H^+ in collisions of C^{3+} with H_2O, using the orientation-average cross sections, calculated with the CTMC-IEM approach. The experimental[24] results for these reactions show that H^+ is the dominant fragment (see Fig. 10), in contrast with the results for H^++H_2O collisions, where H_2O^+ is the major fragment. To discuss this result one must take into account that H_2O^+ is only formed when the electron is removed from the two outermost MOs ($1b_1$, $3a_1$) of H_2O, and a small contribution (8%) if it is removed from the $1b_2$ MO[55]. Accordingly, the corresponding total cross section can be obtained as:

$$\sigma(H_2O^+) = \sigma_{10}(1b_1)+\sigma_{01}(1b_1)+\sigma_{10}(3a_1)+\sigma_{01}(3a_1)+ 0.08[\sigma_{10}(1b_2)+\sigma_{01}(1b_2)] \quad (24)$$

where

$$\sigma_{10}(k) = 2\pi\int_0^\infty bP_{10}^{\rm IEM}(k)\mathrm{d}b;\ \sigma_{01}(k) = 2\pi\int_0^\infty bP_{01}^{\rm IEM}(k)\mathrm{d}b \quad (25)$$

and the orbital contributions to the one electron ionization and capture probabilities, $P_{10}^{\rm IEM}(k), P_{01}^{\rm IEM}(k)$, are defined in eqns (12) and (14). H^+ can be formed in single or multiple electron removal. In particular, after single electron removal[55,56] we have:

$$\sigma^{(1)}(H^+) = 0.22[\sigma_{10}(1b_2)+\sigma_{01}(1b_2)]+ 0.74[\sigma_{10}(2a_1)+\sigma_{01}(2a_1)] \quad (26)$$

Unfortunately, there are no experiments that provide similar fragmentation branching ratios after multiple electron removal. Murakami *et al.* [28] calculated the cross section for two-electron removal, $\sigma^{\rm D}$, in H^++H_2O collisions

$$\sigma^{\rm D} = \sigma_{02}+\sigma_{11}+\sigma_{20} \quad (27)$$

They estimated the fraction of the cross section for production of H^+ that arises from two-electron removal by comparison with the experimental results[12] for fragmentation into H^++H^++O. They found a fraction of $1.2\sigma^{\rm D}$. So that, the cross section after single and double electron removal is

$$\sigma^{(1,2)}(H^+) = \sigma^{(1)}(H^+)+1.2\sigma^{\rm D} \quad (28)$$

The removal of three or more electrons will mainly lead to the complete break out of the molecule, producing two protons by each ionizing event; however, the cross sections for many-electron removal are usually overestimated in the IEM, and Murakami *et al.* [28] suggested to reduce this fraction by an *ad hoc* factor 1/2. Adding the three contributions one obtains

$$\sigma(H^+) = \sigma^{(1)}(H^+)+1.2\sigma^{\rm D}+0.5\sigma^{\rm T} \quad (29)$$

with

$$\sigma^{\rm T} = \sigma_{03}+\sigma_{12}+\sigma_{21}+\sigma_{30} \quad (30)$$

We display in Fig. 10 the cross sections estimated with eqn (24) and (29), compared to the experimental values of Luna and Montenegro[24]. We have also plotted the fractions $\sigma^{(1)}(H^+)$, $\sigma^{(2)}(H^+)$ (eqn (26) and (28)). We observe that the two-electron removal reactions are the largest contributions to the formation of H^+ and, in this model, multiple electron removal explains that $\sigma(H^+)$ is higher than $\sigma(H_2O^+)$. With respect to the comparison with the experiment, we note that the semiempirical model yields absolute cross sections in reasonable agreement with the measured values,

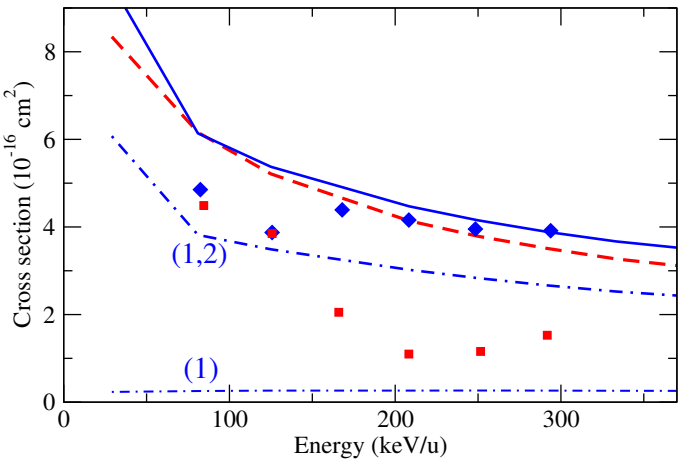

Fig. 10 Total cross sections for formation of H_2O^+ and H^+ in $C^{3+}+H_2O$ collisions. Present results: ——, production of H^+; - - -, production of H_2O^+ [eqn (29)]. Experimental results of Luna and Montenegro [24]: ♦, production of H^+; ■, production of H_2O^+. The two dot-dashed lines with labels are the cross sections estimates for production of H^+ including only the contribution of one-electron processes (1) [$\sigma^{(1)}(H^+)$ of eqn (26)] or (1,2) one- and two-electron processes [$\sigma^{(1,2)}(H^+)$ of eqn (28)].

taking into account the reported uncertainties in the interval 10-12%. However, the model does not reproduce the minimum of $\sigma(H_2O^+)$ at $E = 300$ keV/u. In this case, only single electron removal is relevant and the energy dependence of the one-electron loss cross sections of eqn (26) do not show a minimum at these energies. Moreover, we have found a similar energy dependence of the corresponding cross sections in $Li^{3+}+H_2O$ collisions. One can also note that the CTMC-IEM cross sections $\sigma(H_2O^+)$ are higher than the experimental ones, which is somewhat surprising, given that, in the $Li^{3+}+H_2O$ system, the CTMC-IEM calculation (see Figs. 7 and 8) underestimates both σ_{10} and σ_{01}. A possible explanation of this discrepancy could be the importance of two-electron processes. Auger ionization reduces the single ionization cross section, but it takes place after ionization of an electron from the inner valence orbital $2a_1$, and the ionization from this orbital does not contribute to the formation of H_2O^+. Another two-electron process that could play a role is the excitation of a second electron when one electron is removed from $1b_1$ or $3a_1$ MOs. This process would lead to the formation of an excited electronic state of H_2O^+, which, in contrast with $\tilde{X}^2B_1$ and $\tilde{A}^2A_1$, could fragment, reducing the estimated value of $\sigma(H_2O^+)$.

4 Summary and Conclusions

We have carried out calculations of single electron capture, single ionization and transfer ionization in $X^{q+}+H_2O$ collisions at energies between 20 keV/u and 500 keV/u. We have also considered the net electron production and target electron loss reactions. The calculations were performed in the framework of the semiclassical approximation and using the Franck-Condon approximation. At the energies of the present calculation vibrational effects are small, and the approximation of keeping the target nuclei fixed will not affect the accuracy of the calculation.

Our calculations use the independent electron approximation and three theoretical methods have been employed to solve the one-electron dynamics: a classical mechanics CTMC, and two semiclassical ones, the GridTDSE [43] and AFMO [51]. The three methods use a three-center model potential [27] to describe the four valence molecular orbitals of the water molecule, and two independent electron models are employed (and compared) to produce the many-electron probabilities.

As seen in $H^+ + H_2O$ calculations [27], and explicitly checked in the present study, orientation-averaged cross sections can be well approximated by a single trajectory calculation in the whole range of energies studied that includes the strong perturbation regime where several electrons are released. This is a useful cost-saving strategy, which is particularly useful to avoid lengthy calculations in numerical methods like the GridTDSE.

All methods find similar opacity functions for the electron removal from the valence MOs of the water molecule. In CTMC calculations, the comparison of transition probabilities with quantal ones should be done taking into account all MOs, due to the lack of nodal structure in the initial distributions. In this respect, we find good agreement between the EL and EP total cross sections calculated with the three methods.

The GridTDSE method allows to easily illustrate the electron-capture mechanism by inspecting the electron density along the collision. In this vein, we have shown two snapshots of the electron density for two orbitals. Differences between the electron capture from the $1b_1$ and $1b_2$ orbitals are small for the t_4 projectile trajectory, and we anticipate small differences between random trajectories unless one of them runs along a nodal plane of the molecular orbital.

The main uncertainty of the present calculations of the cross sections σ_{mn} stems from the application of the independent electron approximation. We find relatively large differences in the single electron cross sections σ_{10} and σ_{01} when applying the IEM and IEV interpretations. They correspond to two limits where the multiple electron removal from different subshells is allowed (IEM) or completely forbidden (IEV). These differences indicate that the main limitation of the cross sections in the present and previous calculations comes from the many-electron interpretation. In this respect, the recent work of Jorge *et al.* [34] has introduced a time-dependent potential in the CTMC calculation, that is modified by the electron removal during the collision.

We have shown that, as in previous calculations for H^+ collisions with H_2O, the simple expressions (20) and (22) yield cross sections whose accuracy is directly related to that of the one-electron calculations. Nevertheless, the comparison of the cross sections with the available experiments points to a limitation of the model for collision energies below 50 keV/u for all the one-electron treatments, which is related to the independent electron approximation. Although an all-electron calculation of electron capture is feasible at low energies [57], the connection with the results above 50 keV/u is difficult because the competition of electron capture and ionization processes at these energies (an illustration of this point for ion-atom collisions can be found in the work of Jorge *et al.* [46]).

Finally, we have discussed the importance of many-electron removal in the fragmentation branching ratio. Using a semiempirical model, we have found that the incorporation of two- and

three-electron removal allows us to qualitatively reproduce the experiment of Luna and Montenegro [24] where the production of H^+ higher than that of H_2O^+, although the model does not reproduce the fast decay at high energies of the total cross section for formation of H_2O^+.

Conflicts of interest

There are no conflicts of interest to declare

Acknowledgements

This work has been partially supported by Ministerio de Economía and Competitividad (Spain), project no. FIS2017-84684-R. The computational hosting facilities of the Centro de Computación Científica of UAM are acknowledged.

Notes and references

1 B. Boudaïffa, P. Cloutier, D. Hunting, M. A. Huels and L. Sanche, *Science*, 2000, **287**, 1658–1660.
2 U. Amaldi and G. Kraft, *Rep. Prog. Phys.*, 2005, **68**, 1861–1882.
3 D. Schardt, T. Elsässer and D. Schulz-Ertner, *Rev. Mod. Phys.*, 2010, **82**, 383–425.
4 T. E. Cravens, *Science*, 2002, **296**, 1042–1045.
5 P. S. Rudolph and C. E. Melton, *J. Chem. Phys.*, 1966, **45**, 2227–2232.
6 L. H. Toburen, M. Y. Nakai and R. A. Langley, *Phys. Rev.*, 1968, **171**, 114–122.
7 R. Dagnac, D. Blanc and D. Molina, *J. Phys. B: At. Mol. Opt. Phys.*, 1970, **3**, 1239–1251.
8 L. H. Toburen, W. E. Wilson and R. J. Popowich, *Radiat. Res.*, 1980, **82**, 27–44.
9 M. E. Rudd, T. V. Goffe, R. D. DuBois and L. H. Toburen, *Phys. Rev. A*, 1985, **31**, 492–494.
10 M. E. Rudd, T. V. Goffe and A. Itoh, *Phys. Rev. A*, 1985, **32**, 2128–2133.
11 M. A. Bolorizadeh and M. E. Rudd, *Phys. Rev. A*, 1986, **33**, 888–892.
12 U. Werner, K. Beckord, J. Becker and H. O. Lutz, *Phys. Rev. Lett.*, 1995, **74**, 1962–1965.
13 F. Gobet, S. Eden, B. Coupier, J. Tabet, B. Farizon, M. Farizon, M. J. Gaillard, M. Carré, S. Ouaskit, T. D. Märk and P. Scheier, *Phys. Rev. A*, 2004, **70**, 062716.
14 B. Seredyuk, R. W. McCullough, H. Tawara, H. B. Gilbody, D. Bodewits, R. Hoekstra, A. G. G. M. Tielens, P. Sobocinski, D. Pesic, R. Hellhammer, B. Sulik, N. Stolterfoht, O. Abu-Haija and E. Y. Kamber, *Phys. Rev. A*, 2005, **71**, 022705.
15 A. M. Sayler, M. Leonard, K. D. Carnes, R. Cabrera-Trujillo, B. D. Esry and I. Ben-Itzhak, *J. Phys. B: At. Mol. Opt. Phys.*, 2006, **39**, 1701.
16 H. Luna, A. L. F. de Barros, J. A. Wyer, S. W. J. Scully, J. Lecointre, P. M. Y. Garcia, G. M. Sigaud, A. C. F. Santos, V. Senthil, M. B. Shah, C. J. Latimer and E. C. Montenegro, *Phys. Rev. A*, 2007, **75**, 042711.
17 C. D. Cappello, C. Champion, O. Boudrioua, H. Lekadir, Y. Sato and D. Ohsawa, *Nucl. Instrum. Meth. B*, 2009, **267**, 781 – 790.
18 A. L. F. de Barros, J. Lecointre, H. Luna, M. B. Shah and E. C. Montenegro, *Phys. Rev. A*, 2009, **80**, 012716.
19 S. Martin, L. Chen, R. Brédy, J. Bernard and A. Cassimi, *J. Chem. Phys.*, 2015, **142**, 094306.
20 H. Luna, W. Wolff, E. C. Montenegro, A. C. Tavares, H. J. Lüdde, G. Schenk, M. Horbatsch and T. Kirchner, *Phys. Rev. A*, 2016, **93**, 052705.
21 W. Wolff, H. Luna, R. Schuch, N. D. Cariatore, S. Otranto, F. Turco, D. Fregenal, G. Bernardi and S. Suárez, *Phys. Rev. A*, 2016, **94**, 022712.
22 Simon Wedlund, Cyril, Bodewits, Dennis, Alho, Markku, Hoekstra, Ronnie, Behar, Etienne, Gronoff, Guillaume, Gunell, Herbert, Nilsson, Hans, Kallio, Esa and Beth, Arnaud, *Astron. Astrophys.*, 2019, **630**, A35.
23 G. H. Olivera, C. Caraby, P. Jardin, A. Cassimi, L. Adoui and B. Gervais, *Phys. Med. Biol.*, 1998, **43**, 2347–2360.
24 H. Luna and E. C. Montenegro, *Phys. Rev. Lett.*, 2005, **94**, 043201.
25 J. Suárez, L. Méndez and I. Rabadán, *J. Phys. Chem. Lett.*, 2015, **6**, 72–76.
26 J. Suárez, L. Méndez and I. Rabadán, *Phys. Chem. Chem. Phys.*, 2018, **20**, 28511–28522.
27 C. Illescas, L. F. Errea, L. Méndez, B. Pons, I. Rabadán and A. Riera, *Phys. Rev. A*, 2011, **83**, 052704.
28 M. Murakami, T. Kirchner, M. Horbatsch and H. J. Lüdde, *Phys. Rev. A*, 2012, **85**, 052713.
29 L. F. Errea, C. Illescas, L. Méndez, B. Pons, I. Rabadán and A. Riera, *Phys. Rev. A*, 2007, **76**, 040701(R).
30 T. Liamsuwan and H. Nikjoo, *Phys. Med. Biol.*, 2013, **58**, 641.
31 L. F. Errea, C. Illescas, L. Méndez and I. Rabadán, *Phys. Rev. A*, 2013, **87**, 032709.
32 S. T. S. Kovács, P. Herczku, Z. Juhász, L. Sarkadi, L. Gulyás and B. Sulik, *Phys. Rev. A*, 2016, **94**, 012704.
33 S. T. S. Kovács, P. Herczku, Z. Juhász, L. Sarkadi, L. Gulyás and B. Sulik, *Phys. Rev. A*, 2017, **96**, 032704.
34 A. Jorge, M. Horbatsch, C. Illescas and T. Kirchner, *Phys. Rev. A*, 2019, **99**, 062701.
35 O. Boudrioua, C. Champion, C. DalCappello and Y. V. Popov, *Phys. Rev. A*, 2007, **75**, 022720.
36 C. Champion, O. Boudrioua, C. Dal Cappello, Y. Sato and D. Ohsawa, *Phys. Rev. A*, 2007, **75**, 032724.
37 M. Bernal and J. Liendo, *Nucl. Instrum. Meth. B*, 2007, **262**, 1 – 6.
38 C. C. Montanari and J. E. Miraglia, *J. Phys. B: At. Mol. Opt. Phys.*, 2013, **47**, 015201.
39 C. A. Tachino, J. M. Monti, O. A. Fojón, C. Champion and R. D. Rivarola, *J. Phys. B: At. Mol. Opt. Phys.*, 2014, **47**, 035203.
40 M. A. Quinto, P. R. Montenegro, J. M. Monti, O. A. Fojón and R. D. Rivarola, *J. Phys. B: At. Mol. Opt. Phys.*, 2018, **51**, 165201.
41 M. Murakami, T. Kirchner, M. Horbatsch and H. J. Lüdde, *Phys. Rev. A*, 2012, **85**, 052704.

42 M. Murakami, T. Kirchner, M. Horbatsch and H. J. Lüdde, *Phys. Rev. A*, 2012, **86**, 022719.
43 L. Errea, C. Illescas, L. Méndez, I. Rabadán and J. Suárez, *Chem. Phys.*, 2015, **462**, 17 – 22.
44 A. Jorge, J. Suárez, C. Illescas, L. F. Errea and L. Méndez, *Phys. Rev. A*, 2016, **94**, 032707.
45 J. Suarez, S. Farantos, S. Stamatiadis and L. Lathouwers, *Comput. Phys. Commun.*, 2009, **180**, 2025 – 2033.
46 A. Jorge, C. Illescas, L. Méndez and I. Rabadán, *J. Phys. Chem. A*, 2018, **122**, 2523–2534.
47 T. Kirchner, L. Gulyás, H. J. Lüdde, E. Engel and R. M. Dreizler, *Phys. Rev. A*, 1998, **58**, 2063.
48 B. H. Bransden and M. H. C. McDowell, *Charge Exchange and the Theory of Ion-Atom Collisions*, Oxford, Clarendon, 1992.
49 X. Urbain, N. de Ruette, V. M. Andrianarijaona, M. F. Martin, L. F. Menchero, L. F. Errea, L. Méndez, I. Rabadán and B. Pons, *Phys. Rev. Lett.*, 2013, **111**, 203201
50 A. Hoy and P. Bunker, *J. Mol. Spectrosc.*, 1979, **74**, 1 – 8.
51 P. M. M. Gabás, L. F. Errea, L. Méndez and I. Rabadán, *Phys. Rev. A*, 2012, **85**, 012702.
52 R. Abrines and I. C. Percival, *Proc. Phys. Soc.*, 1966, **88**, 861–872.
53 L. F. Errea, C. Harel, H. Jouin, L. Méndez, B. Pons, A. Riera and I. Sevila, *Phys. Rev. A*, 2002, **65**, 022711.
54 C. Lanczos, *J. Res. Natl. Bur. Stand. B*, 1950, **45**, 255–282.
55 K. Tan, C. Brion, P. V. der Leeuw and M. van der Wiel, *Chem. Phys.*, 1978, **29**, 299 – 309.
56 E. C. Montenegro, *J. Phys. Conf. Ser.*, 2009, **194**, 012049.
57 S. Mada, K. N. Hida, M. Kimura, L. Pichl, H.-P. Liebermann, Y. Li and R. J. Buenker, *Phys. Rev. A*, 2007, **75**, 022706.